

Reconstruction of Liquid–Liquid Extraction Performance in Parallel Microflows

Dhruv Jalan (23110099), Antariksh Dongre (23110031), Suyog Latke (23110325)

dhruv.jalan@iitgn.ac.in, antariksh.dongre@iitgn.ac.in, suyog.latke@iitgn.ac.in

*Department of Chemical Engineering
Indian Institute of Technology Gandhinagar*

Course Project Report — CL314: Separation Processes

Instructor: Prof. Karthik Subramaniam Pushpavanam

Abstract—This report recreates the fluid-flow and mass-transfer models used to study liquid–liquid extraction in microchannels, following the work of Vir *et al.* It examines three flow arrangements: core–annular flow in a round channel, two-dimensional stratified flow in a rectangular channel, and a simplified one-dimensional stratified case (infinite parallel plates). For each setup, the velocity is derived from Navier -Stokes and combined with the solute transport equation. Numerical solutions are obtained using the Method of Lines.

INTRODUCTION

Liquid–liquid extraction in microchannels works well because microscale flows create a large interfacial area and short diffusion distances. When two immiscible liquids flow either side-by-side (*stratified*) or one inside the other (*core–annular*), they form a stable interface where solute transfer occurs.

In this work, we recreate the hydrodynamic and mass-transfer models developed by Picardo *et al.* and use them to compare extraction performance in three microchannel configurations:

- 1) **1-D stratified flow** between parallel plates,
- 2) **2-D stratified flow** in a rectangular channel, and
- 3) **Core–annular flow** in a circular channel.

By deriving the velocity profile, solving the mass-transport equations, and comparing the predicted extraction trends, we show how channel geometry and flow behavior together influence liquid–liquid extraction performance in microchannel systems. Finally we do mass balance verification of all the concentration profiles to validate our results.

PROBLEM SETUP

This project recreates the extraction behaviour of two immiscible liquids flowing together in microchannels, following the model of Vir *et al.* The goal is to understand how channel shape, flow arrangement, and fluid properties affect solute transfer across a stable interface as the liquids move downstream. Three flow setups are studied: core–annular flow in a circular channel, two-dimensional stratified flow in a rectangular channel, and a simplified one-dimensional stratified case representing channels with very large aspect ratios.

In each configuration, the solute starts entirely in the carrier phase and diffuses into the solvent while both phases are carried forward by laminar flow. A common set of assumptions—steady, fully developed flow, a flat interface, negligible axial diffusion, constant properties, and fast interfacial equilibrium—allows fair comparison across geometries. The inputs include flow rates, viscosity and diffusivity ratios, the partition coefficient, and geometric parameters, while the outputs are the predicted velocity fields, concentration profiles, and extraction performance.

MODELING STEPS- DERIVATIONS + METHODS

In this section, we outline the mathematical models used to describe the velocity fields and mass-transfer behavior in the three microchannel geometries considered: one-dimensional (1-D) stratified flow, two-dimensional (2-D) stratified flow, and core–annular flow. Our goal is not to reproduce the full derivations presented in the reference study, but to present the final governing equations, the assumptions behind them, and the physical meaning of each term. All symbols introduced below follow the notation used in Vir *et al.* [1].

I. MATHEMATICAL METHOD AND ASSUMPTIONS

A. Common Assumptions and Notation

All models rely on the following assumptions:

- Steady, incompressible, laminar, fully developed flow.
- Two immiscible Newtonian liquids with constant viscosity μ_i and diffusivity D_i .
- A flat, stationary interface separating the phases.
- Axial convection dominates over axial diffusion (high Peclet number), so diffusion occurs only in the transverse direction(s).
- Instantaneous thermodynamic equilibrium at the interface, with distribution coefficient k .

We denote:

- v_i — velocity field in phase i .
- c_i — solute concentration in phase i .
- Q_i — volumetric flow rate of phase i .

- D_i — molecular diffusivity.
- μ_i — dynamic viscosity.
- α — holdup (fraction of channel cross-section occupied by a phase).
- Pe_i — Peclet number of phase i .

Dimensionless ratios used throughout are:

$$\mu_r = \frac{\mu_2}{\mu_1}, \quad D_r = \frac{D_2}{D_1}, \quad Q_r = \frac{Q_2}{Q_1}. \quad (1)$$

B. Method of Lines (MOL)

The simulation utilizes the Method of Lines (MOL) to solve the steady-state convection-diffusion equations governing mass transfer in the microchannel. The MOL is a semi-analytical technique that converts a Partial Differential Equation (PDE) into a system of coupled Ordinary Differential Equations (ODEs) by discretizing all spatial dimensions except for one. In this work, the flow directions (x or z) is treated as a pseudo-time variable, while the directions that are perpendicular (y or r) are discretized using finite differences.

1) **Governing Equations:** The general steady-state convection-diffusion equation for a species concentration C in a flow field with velocity v is given by:

$$v(y, z) \frac{\partial C}{\partial x} = D_r \left(\frac{\partial^2 C}{\partial y^2} + \frac{\partial^2 C}{\partial z^2} \right) \quad (2)$$

2) **Spatial Discretization (in the direction perpendicular to flow):** The perpendicular domain is discretized into a grid of N nodes. At each interior node i , the Laplacian operator is approximated using a second-order central difference scheme. For a 1D transverse coordinate y , the approximation is:

$$\frac{\partial^2 C}{\partial y^2} \Big|_i \approx \frac{C_{i+1} - 2C_i + C_{i-1}}{\Delta y^2} \quad (3)$$

$$\frac{\partial C}{\partial y} \Big|_i \approx \frac{C_{i+1} - C_{i-1}}{2\Delta y} \quad (4)$$

Substituting this into the governing equation transforms the PDE into a system of N coupled ODEs:

$$\frac{dC_i}{dx} = \frac{D}{v_i} \left[\frac{C_{i+1} - 2C_i + C_{i-1}}{\Delta y^2} \right] \quad (5)$$

3) **Time Integration:** The resulting system of ODEs is stiff due to the diffusive terms (where the eigenvalues scale with $1/\Delta y^2$). Consequently, the system is integrated along the channel length using a Backward Differentiation Formula (BDF) method, an implicit solver suitable for stiff problems, as implemented in the `scipy.integrate.solve_ivp` routine.

II. DERIVATION

1-D Stratified Flow Model

The 1-D stratified model represents two immiscible liquids flowing in parallel between two infinite flat plates separated by a distance H . Phase-1 (carrier) occupies $0 \leq y \leq \alpha_s$, while phase-2 (solvent) occupies $\alpha_s \leq y \leq 1$. A schematic of the domain is shown in Fig. 1.

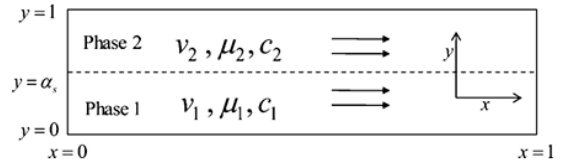


Fig. 1. Schematic of the 1-D stratified flow model. Phase-1 occupies $0 \leq y \leq \alpha_s$ and phase-2 occupies $\alpha_s \leq y \leq 1$.

Reduction of Navier-Stokes: We begin with the incompressible Navier-Stokes equations,

$$\rho_i (\mathbf{u}_i \cdot \nabla \mathbf{u}_i) = -\nabla p + \mu_i \nabla^2 \mathbf{u}_i, \quad \nabla \cdot \mathbf{u}_i = 0. \quad (6)$$

Using the standard assumptions of 1-D laminar flow:

$$u_i = 0, \quad w_i = 0, \quad v_i = v_i(y), \quad \frac{\partial}{\partial x} = 0, \quad \frac{\partial}{\partial t} = 0,$$

the x -momentum equation simplifies to

$$\mu_i \frac{d^2 v_i^*}{dy^{*2}} = \frac{\partial p}{\partial x}. \quad (7)$$

Non-dimensionalisation:

$$y = \frac{y^*}{H}, \quad v_i = \frac{v_i^*}{v_{i,\text{ch}}}, \quad v_{i,\text{ch}} = \frac{\tilde{Q}_i}{H},$$

where \tilde{Q}_i is volumetric flow rate per unit depth. Using

$$\frac{d}{dy^*} = \frac{1}{H} \frac{d}{dy},$$

Eq. (7) becomes

$$\frac{d^2 v_i}{dy^2} = \frac{\left(\frac{\partial p}{\partial x}\right) H^3}{\mu_i \tilde{Q}_i} = G_i.$$

Thus the dimensionless momentum equations in both phases are

$$\frac{d^2 v_i}{dy^2} = G_i, \quad i = 1, 2. \quad (8)$$

Boundary and Interface Conditions: No-slip at the walls:

$$v_1(0) = 0, \quad v_2(1) = 0. \quad (9)$$

Velocity continuity at the interface ($y = \alpha_s$):

$$v_1(\alpha_s) = \tilde{Q}_r v_2(\alpha_s), \quad \tilde{Q}_r = \frac{\tilde{Q}_2}{\tilde{Q}_1}. \quad (10)$$

Shear-stress continuity:

$$\left. \frac{dv_1}{dy} \right|_{y=\alpha_s} = \tilde{Q}_r \mu_r \left. \frac{dv_2}{dy} \right|_{y=\alpha_s}, \quad \mu_r = \frac{\mu_2}{\mu_1}. \quad (11)$$

General Solutions: Integrating Eq. (8) twice,

$$v_1(y) = \frac{G_1}{2}y^2 + C_{11}y + C_{12}, \quad (12)$$

$$v_2(y) = \frac{G_2}{2}y^2 + C_{21}y + C_{22}. \quad (13)$$

Applying $v_1(0) = 0$ gives $C_{12} = 0$. Applying $v_2(1) = 0$ gives $C_{22} = -\frac{G_2}{2} - C_{21}$.

Thus,

$$v_1(y) = \frac{G_1}{2}y^2 + C_{11}y, \quad (14)$$

$$v_2(y) = \frac{G_2}{2}y^2 + C_{21}y - \frac{G_2}{2} - C_{21}. \quad (15)$$

Solving Interface Conditions: Velocity continuity (10) gives:

$$\frac{G_1}{2}\alpha_s^2 + C_{11}\alpha_s = \tilde{Q}_r \left[\frac{G_2}{2}\alpha_s^2 + C_{21}\alpha_s - \frac{G_2}{2} - C_{21} \right]. \quad (16)$$

Shear-stress continuity (11) gives:

$$G_1\alpha_s + C_{11} = \tilde{Q}_r\mu_r(G_2\alpha_s + C_{21}). \quad (17)$$

Solving Eqs. (16)–(17) yields closed-form expressions for C_{11} and C_{21} . Substituting them back gives the final velocity profiles.

Final Paper-Style Velocity Expressions: After algebraic reduction (matching the form used in the reference study), the 1-D velocity profiles become:

Phase-1::

$$v_1(y) = \frac{G_1 y^2}{2} + \mu_2 \left[\frac{G_2 \tilde{Q}_r (\alpha_s^2 - 1) - G_1 \alpha_s^2}{2(\mu_1 - \alpha_s \mu_1 + \alpha_s \mu_2)} \right] y. \quad (36)$$

Phase-2::

$$v_2(y) = \frac{G_2 y^2}{2} + \mu_1 \left[\frac{G_1 \alpha_s^2 - G_2 (\alpha_s^2 - 1) \tilde{Q}_r}{2 \tilde{Q}_r [(\alpha_s - 1) \mu_1 - \alpha_s \mu_2]} \right] y \quad (18)$$

$$+ \left[\frac{G_2 \alpha_s \tilde{Q}_r [(\alpha_s - 1) \mu_1 + \mu_2] - G_1 \alpha_s^2 \mu_1}{2 \tilde{Q}_r [(\alpha_s - 1) \mu_1 - \alpha_s \mu_2]} \right]. \quad (37)$$

Equations (36)–(37) match exactly the expressions reported in the reference paper.

A. 2-D Stratified Flow Model

The 2-D stratified model describes two immiscible liquids flowing in a rectangular microchannel of width H (in y) and depth d (in z). Phase-1 (carrier) occupies $0 \leq y \leq \alpha_s$ and phase-2 (solvent) occupies $\alpha_s \leq y \leq 1$, where $\alpha_s = h/H$ is the dimensionless interface position. A schematic of the configuration is shown in Fig. 2.

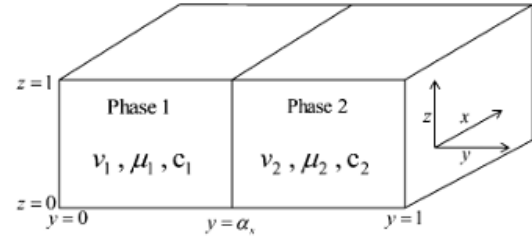


Fig. 2. Schematic of 2-D stratified flow in a rectangular microchannel of width H and depth d . Phase-1 occupies $0 \leq y \leq \alpha_s$ and phase-2 occupies $\alpha_s \leq y \leq 1$.

Reduction of Navier-Stokes: Starting from the incompressible Navier-Stokes equations,

$$\rho_i \left(\frac{\partial \mathbf{u}_i}{\partial t} + \mathbf{u}_i \cdot \nabla \mathbf{u}_i \right) = -\nabla p + \mu_i \nabla^2 \mathbf{u}_i, \quad \nabla \cdot \mathbf{u}_i = 0,$$

we assume:

- steady flow ($\partial/\partial t = 0$),
- unidirectional, fully developed velocity in x : $\mathbf{u}_i = (v_i(x), 0, 0)$ with $\partial v_i / \partial x = 0$,
- no body forces and low Reynolds number (negligible inertia).

Under these assumptions the x -momentum equation reduces to

$$\mu_i \left(\frac{\partial^2 v_i^*}{\partial y^{*2}} + \frac{\partial^2 v_i^*}{\partial z^{*2}} \right) = \frac{\partial p}{\partial x}, \quad i = 1, 2, \quad (19)$$

where $\partial p / \partial x$ is constant and the same in both phases.

Non-Dimensionalisation: We define dimensionless variables

$$y = \frac{y^*}{H}, \quad z = \frac{z^*}{d}, \quad v_i = \frac{v_i^*}{v_{i,\text{ch}}},$$

with characteristic velocities

$$v_{1,\text{ch}} = \frac{Q_1}{H^2}, \quad v_{2,\text{ch}} = \frac{Q_2}{H^2},$$

where Q_i are volumetric flow rates.

The aspect ratio and ratios of properties are

$$\lambda = \frac{H}{d}, \quad Q_r = \frac{Q_2}{Q_1}, \quad \mu_r = \frac{\mu_2}{\mu_1}.$$

We introduce the dimensionless pressure-gradient parameters

$$G_1 = \frac{(\partial p / \partial x) H^4}{Q_1 \mu_1}, \quad G_2 = \frac{(\partial p / \partial x) H^4}{Q_2 \mu_2}.$$

Substituting the scales into (19) and dropping the asterisks yields the 2-D Poisson equations

$$\frac{\partial^2 v_1}{\partial y^2} + \lambda^2 \frac{\partial^2 v_1}{\partial z^2} = G_1, \quad 0 \leq y \leq \alpha_s, \quad 0 \leq z \leq 1, \quad (20)$$

$$\frac{\partial^2 v_2}{\partial y^2} + \lambda^2 \frac{\partial^2 v_2}{\partial z^2} = G_2, \quad \alpha_s \leq y \leq 1, \quad 0 \leq z \leq 1. \quad (21)$$

Boundary and Interface Conditions:

No-slip at walls:

$$\begin{aligned} v_1(0, z) &= 0, & v_2(1, z) &= 0, \\ v_i(y, 0) &= 0, & v_i(y, 1) &= 0, \quad i = 1, 2. \end{aligned}$$

Interface at $y = \alpha_s$: Velocity continuity:

$$v_1(\alpha_s, z) = Q_r v_2(\alpha_s, z). \quad (22)$$

Shear-stress continuity:

$$\left. \frac{\partial v_1}{\partial y} \right|_{y=\alpha_s} = Q_r \mu_r \left. \frac{\partial v_2}{\partial y} \right|_{y=\alpha_s}. \quad (23)$$

Velocity Field via Eigenfunction Expansion: To satisfy the no-slip conditions at $z = 0$ and $z = 1$, we expand the velocity as a sine series in z :

$$v_i(y, z) = \sum_{n=1}^{\infty} f_{in}(y) \sin(n\pi z).$$

Substituting into (20)–(21) gives, for each mode n ,

$$\frac{d^2 f_{1n}}{dy^2} - \lambda^2 (n\pi)^2 f_{1n} = \frac{2G_1[(-1)^n - 1]}{n^3 \pi^3 \lambda^2}, \quad (24)$$

$$\frac{d^2 f_{2n}}{dy^2} - \lambda^2 (n\pi)^2 f_{2n} = \frac{2G_2[(-1)^n - 1]}{n^3 \pi^3 \lambda^2}. \quad (25)$$

The general solutions of these ODEs are

$$f_{in}(y) = A_{1n} \cosh(n\pi\lambda y) + A_{2n} \sinh(n\pi\lambda y) + \frac{2G_i[(-1)^n - 1]}{n^3 \pi^3 \lambda^2}.$$

Imposing the wall conditions at $y = 0$ and $y = 1$, together with (22)–(23), determines the constants $A_{1n}, A_{2n}, A_{3n}, A_{4n}$ (one pair for each phase).

The resulting velocity fields can be written as

$$v_1(y, z) = \sum_{n=1}^{\infty} \left[\frac{2G_1[(-1)^n - 1]}{n^3 \pi^3 \lambda^2} \right] \left(A_{1n} \cosh(n\pi\lambda y) + \right. \quad (26)$$

$$\left. A_{2n} \sinh(n\pi\lambda y) + 1 \right) \sin(n\pi z), \quad (27)$$

$$v_2(y, z) = \sum_{n=1}^{\infty} \left[\frac{2G_2[(-1)^n - 1]}{n^3 \pi^3 \lambda^2} \right] \left(A_{3n} \cosh(n\pi\lambda y) + \right. \quad (28)$$

$$\left. A_{4n} \sinh(n\pi\lambda y) + 1 \right) \sin(n\pi z). \quad (29)$$

In practice, retaining the first $\mathcal{O}(10)$ terms provides sufficient accuracy for the subsequent mass-transfer calculations.

Mass-Transfer Equations: For each phase, the dimensional convection-diffusion equation (neglecting axial diffusion) is

$$v_i^*(y^*, z^*) \frac{\partial c_i^*}{\partial x} = D_i \left(\frac{\partial^2 c_i^*}{\partial y^{*2}} + \frac{\partial^2 c_i^*}{\partial z^{*2}} \right).$$

We non-dimensionalise

$$x = \frac{x^*}{L}, \quad y = \frac{y^*}{H}, \quad z = \frac{z^*}{d}, \quad c_i = \frac{c_i^*}{c_{in}},$$

and use the same velocity scales $v_{i,ch}$ as before.

The 2-D Péclet numbers are

$$\text{Pe}_1^{2D} = \frac{Q_1}{D_1 L}, \quad \text{Pe}_2^{2D} = \frac{Q_2}{D_2 L}.$$

The dimensionless species balances become

$$\frac{\partial c_1}{\partial x} = \left(\frac{1}{v_1} \right) \left(\frac{1}{\text{Pe}_1^{2D}} \right) \left[\frac{\partial^2 c_1}{\partial y^2} + \lambda^2 \frac{\partial^2 c_1}{\partial z^2} \right], \quad (30)$$

$$\frac{\partial c_2}{\partial x} = \left(\frac{1}{v_2} \right) \left(\frac{1}{\text{Pe}_2^{2D}} \right) \left[\frac{\partial^2 c_2}{\partial y^2} + \lambda^2 \frac{\partial^2 c_2}{\partial z^2} \right]. \quad (31)$$

F. Mass-Transfer Boundary and Interface Conditions:

Walls: No normal flux at all solid boundaries:

$$\frac{\partial c_i}{\partial y} = 0 \text{ at } y = 0, 1, \quad \frac{\partial c_i}{\partial z} = 0 \text{ at } z = 0, 1, \quad i = 1, 2.$$

Interface at $y = \alpha_s$: Thermodynamic equilibrium:

$$c_2 = k c_1,$$

Flux continuity:

$$\frac{\partial c_1}{\partial y} = D_r \frac{\partial c_2}{\partial y}, \quad D_r = \frac{D_2}{D_1}.$$

These equations, together with the inlet conditions ($c_1 = 1, c_2 = 0$ at $x = 0$), define the 2-D stratified mass-transfer model used in our simulations.

B. Core–Annular Flow Model

In this geometry, two immiscible liquids flow through a circular microchannel of radius R_0 . The inner liquid (core, subscript c) occupies $0 \leq r \leq a$, where $a = R_i/R_0$ is the dimensionless core radius, and the outer liquid (annulus, subscript a) occupies $a \leq r \leq 1$. The flow is driven by a constant axial pressure gradient $\partial \tilde{p}/\partial \tilde{z}$. A schematic is shown in Fig. 3.

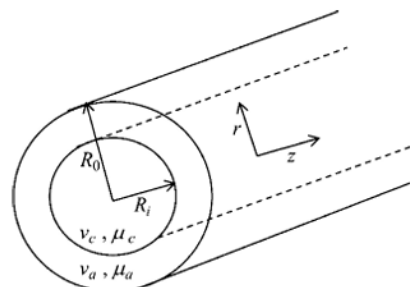


Fig. 3. Schematic of core–annular liquid–liquid flow in a circular microchannel of radius R_0 , with core radius $R_i = aR_0$.

A. Reduction of Navier–Stokes in Cylindrical Coordinates:
We work in cylindrical coordinates $(\tilde{r}, \tilde{\theta}, \tilde{z})$. For an incompressible Newtonian fluid, the axial (\tilde{z}) momentum equation is

$$\begin{aligned} \rho \left(\frac{\partial \tilde{v}_z}{\partial t} + \tilde{v}_r \frac{\partial \tilde{v}_z}{\partial \tilde{r}} + \frac{\tilde{v}_\theta}{\tilde{r}} \frac{\partial \tilde{v}_z}{\partial \tilde{\theta}} + \tilde{v}_z \frac{\partial \tilde{v}_z}{\partial \tilde{z}} \right) = & - \frac{\partial \tilde{p}}{\partial \tilde{z}} \\ & + \mu \left[\frac{1}{\tilde{r}} \frac{\partial}{\partial \tilde{r}} \left(\tilde{r} \frac{\partial \tilde{v}_z}{\partial \tilde{r}} \right) \right]_c = \tilde{v}_a \text{ gives} \\ & + \mu \left[\frac{1}{\tilde{r}^2} \frac{\partial^2 \tilde{v}_z}{\partial \tilde{\theta}^2} \right] \\ & + \mu \left[\frac{\partial^2 \tilde{v}_z}{\partial \tilde{z}^2} \right]. \end{aligned} \quad (32)$$

For core–annular flow we assume:

- steady flow: $\partial(\cdot)/\partial t = 0$,
- axisymmetry: $\partial(\cdot)/\partial \tilde{\theta} = 0$,
- fully developed, unidirectional flow: $\tilde{v}_r = 0$, $\tilde{v}_\theta = 0$, $\tilde{v}_z = \tilde{v}_i(\tilde{r})$, $\partial \tilde{v}_i / \partial \tilde{z} = 0$,
- no body forces and low Reynolds number (negligible inertia).

All convective terms vanish, and the axial momentum equation simplifies to

$$0 = - \frac{\partial \tilde{p}}{\partial \tilde{z}} + \mu_i \left[\frac{1}{\tilde{r}} \frac{d}{d\tilde{r}} \left(\tilde{r} \frac{d\tilde{v}_i}{d\tilde{r}} \right) \right], \quad i \in \{c, a\}. \quad (33)$$

B. Non-Dimensionalisation: We introduce characteristic velocities

$$v_{c,\text{ch}} = \frac{Q_c}{\pi R_0^2}, \quad v_{a,\text{ch}} = \frac{Q_a}{\pi R_0^2},$$

and define

$$r = \frac{\tilde{r}}{R_0}, \quad z = \frac{\tilde{z}}{L}, \quad v_c = \frac{\tilde{v}_c}{v_{c,\text{ch}}}, \quad v_a = \frac{\tilde{v}_a}{v_{a,\text{ch}}}.$$

The viscosity and flow-rate ratios are

$$\mu_r = \frac{\mu_a}{\mu_c}, \quad Q_r = \frac{Q_a}{Q_c}.$$

Using $\tilde{r} = R_0 r$ and $\tilde{v}_i = v_{i,\text{ch}} v_i$ in (33) leads to

$$\frac{v_{i,\text{ch}}}{R_0^2} \frac{1}{r} \frac{d}{dr} \left(r \frac{dv_i}{dr} \right) = \frac{1}{\mu_i} \frac{\partial \tilde{p}}{\partial \tilde{z}}. \quad (34)$$

We define

$$G_i = \frac{R_0^2}{\mu_i v_{i,\text{ch}}} \frac{\partial \tilde{p}}{\partial \tilde{z}} = \frac{\pi R_0^4}{\mu_i Q_i} \frac{\partial \tilde{p}}{\partial \tilde{z}}, \quad i \in \{c, a\},$$

so that the dimensionless momentum equations become

$$\frac{1}{r} \frac{d}{dr} \left(r \frac{dv_c}{dr} \right) = G_c, \quad 0 \leq r \leq a, \quad (35)$$

$$\frac{1}{r} \frac{d}{dr} \left(r \frac{dv_a}{dr} \right) = G_a, \quad a \leq r \leq 1. \quad (36)$$

Because both phases experience the same physical pressure gradient $\partial \tilde{p} / \partial \tilde{z}$, the forcing parameters satisfy

$$\mu_c v_{c,\text{ch}} G_c = \mu_a v_{a,\text{ch}} G_a \Rightarrow G_c = \mu_r Q_r G_a.$$

C. Boundary and Interface Conditions:

Core symmetry at $r = 0$:

$$\left. \frac{dv_c}{dr} \right|_{r=0} = 0.$$

No slip at the wall $r = 1$:

$$v_a(1) = 0.$$

$$v_c(a) = Q_r v_a(a). \quad (37)$$

Shear-stress continuity at $r = a$:

$$\mu_c \left. \frac{dv_c}{dr} \right|_{r=a} = \mu_a \left. \frac{dv_a}{dr} \right|_{r=a} \Rightarrow \left. \frac{dv_c}{dr} \right|_{r=a} = \mu_r Q_r \left. \frac{dv_a}{dr} \right|_{r=a}.$$

D. Velocity Profiles: Integrating (35) and enforcing regularity at $r = 0$ (no logarithmic singularity) gives a purely quadratic core profile:

$$v_c(r) = \frac{G_c}{4} r^2 + C_c, \quad 0 \leq r \leq a. \quad (38)$$

The general solution of (36) is

$$v_a(r) = \frac{G_a}{4} r^2 + C_{a1} \ln r + C_{a2}, \quad a \leq r \leq 1. \quad (39)$$

The wall condition $v_a(1) = 0$ implies

$$C_{a2} = -\frac{G_a}{4}.$$

Using velocity and shear continuity at $r = a$, together with $G_c = \mu_r Q_r G_a$, eliminates the logarithmic term ($C_{a1} = 0$) and yields simple parabolic profiles. The final dimensionless velocity fields are

$$v_a(r) = \frac{G_a}{4} (r^2 - 1), \quad (40)$$

$$v_c(r) = \frac{G_a Q_r}{4} (a^2 - 1) + \frac{G_c}{4} (r^2 - a^2), \quad (41)$$

which are the forms used in the subsequent mass-transfer model.

E. Mass-Transfer Model: Let $\tilde{c}_i(\tilde{r}, \tilde{z})$ denote the solute concentration in phase $i \in \{c, a\}$. Assuming steady state, axisymmetry, convection only in the axial direction, and radial diffusion only, the dimensional convection–diffusion equation is

$$\tilde{v}_i(\tilde{r}) \frac{\partial \tilde{c}_i}{\partial \tilde{z}} = D_i \left[\frac{1}{\tilde{r}} \frac{\partial}{\partial \tilde{r}} \left(\tilde{r} \frac{\partial \tilde{c}_i}{\partial \tilde{r}} \right) \right], \quad (42)$$

where D_i is the molecular diffusivity in phase i .

We non-dimensionalise as

$$c_i = \frac{\tilde{c}_i}{c_{\text{in}}}, \quad r = \frac{\tilde{r}}{R_0}, \quad z = \frac{\tilde{z}}{L},$$

with $v_i = \tilde{v}_i / v_{i,\text{ch}}$ as defined earlier.

The mass Pécelt numbers are

$$\text{Pe}_c = \frac{v_{c,\text{ch}} R_0^2}{D_c L} = \frac{Q_c}{\pi D_c L}, \quad \text{Pe}_a = \frac{v_{a,\text{ch}} R_0^2}{D_a L} = \frac{Q_a}{\pi D_a L}.$$

The dimensionless mass-transfer equations become

$$\frac{\partial c_c}{\partial z} = \frac{1}{v_c(r) Pe_c} \left(\frac{\partial^2 c_c}{\partial r^2} + \frac{1}{r} \frac{\partial c_c}{\partial r} \right), \quad 0 \leq r \leq a, \quad (43)$$

$$\frac{\partial c_a}{\partial z} = \frac{1}{v_a(r) Pe_a} \left(\frac{\partial^2 c_a}{\partial r^2} + \frac{1}{r} \frac{\partial c_a}{\partial r} \right), \quad a \leq r \leq 1. \quad (44)$$

F. Mass-Transfer Boundary and Interface Conditions:

Wall and centreline:

$$\frac{\partial c_c}{\partial r} \Big|_{r=0} = 0, \quad \frac{\partial c_a}{\partial r} \Big|_{r=1} = 0.$$

Interface at $r = a$: Local equilibrium:

$$c_c(a, z) = k_{ca} c_a(a, z),$$

where k_{ca} is the distribution coefficient between core and annulus.

Flux continuity:

$$\frac{\partial c_c}{\partial r} \Big|_{r=a} = D_r \frac{\partial c_a}{\partial r} \Big|_{r=a}, \quad D_r = \frac{D_a}{D_c}.$$

Inlet conditions at $z = 0$: If the carrier fluid is in the core:

$$c_c(r, 0) = 1, \quad c_a(r, 0) = 0.$$

If the carrier fluid is in the annulus:

$$c_a(r, 0) = 1, \quad c_c(r, 0) = 0.$$

The governing equations derived above fully describe the velocity and mass-transfer behavior for all three microchannel geometries. These models form the foundation for the numerical simulations presented in the next section, where we compute concentration fields, extraction efficiencies, and compare the trends with those reported by Vir *et al.* [1].

RESULTS AND MODEL VALIDATION

In this section, we compare the velocity profiles, mass-transfer distributions, and extraction-performance metrics obtained from our reconstructed models with the corresponding results reported by Vir *et al.* [1]. The comparison spans all three geometries studied in the paper—1-D stratified flow, 2-D stratified flow, and core–annular flow

C. Core–Annular Flow: Velocity Profile

Figure 4 shows the comparison between our computed core–annular velocity profile and the reference result. Both curves display the characteristic parabolic core region, a steeper annular gradient, and a smooth transition across the interface. The model accurately captures:

- the interface position,
- the curvature and peak velocity inside the core,
- the expected slope change dictated by shear-stress continuity.

In the plot we have obtained in Python, the maximum value obtained is crossing 3.5, where as in the plot given in the paper, the maximum value is clipped at 3.0. This shows our inconsistencies in modelling.

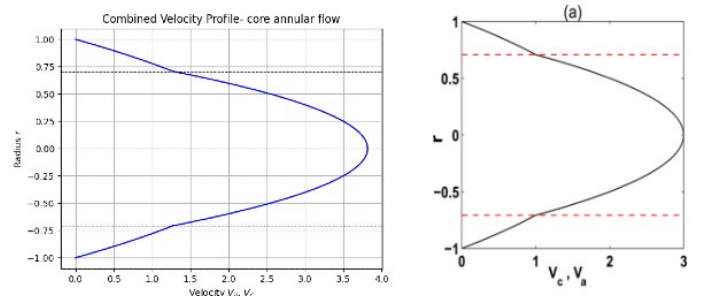


Fig. 4. Comparison of dimensionless velocity profiles for core–annular flow. Left: reconstructed result; Right: reference result from Vir *et al.* [1].

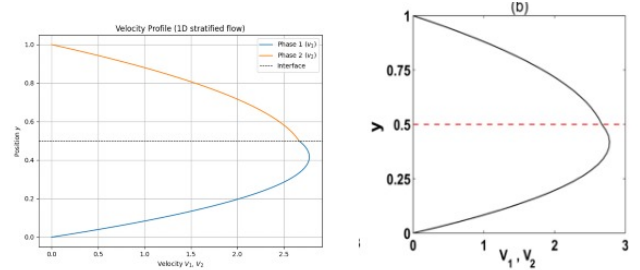


Fig. 5. Comparison of the reconstructed 1-D stratified velocity profile (left) with the reference plot from Vir *et al.* (right).

D. 1-D Stratified Flow: Velocity Profile

Figure 5 shows the velocity field obtained from our 1-D stratified model. Each phase forms a distinct parabolic profile, with the less viscous fluid developing the larger peak velocity and the interface clearly identified at the correct location.

The reconstructed profile matches exactly with the reference plot of Vir *et al.*. As noted in the original study, stratified flow always places the maximum axial velocity in the less viscous phase, and this behaviour is accurately reproduced in our results.

E. 2-D Stratified Flow: Velocity Contours

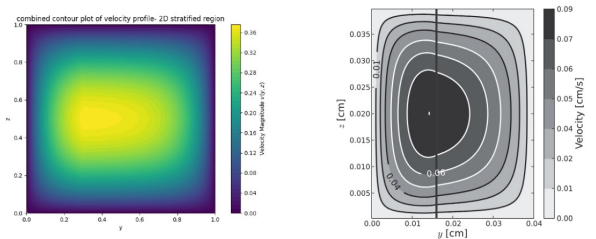


Fig. 6. Velocity magnitude contours for the 2-D stratified flow model.

Figure 6 shows the velocity magnitude distribution predicted by the 2-D stratified flow model. The contours exhibit the characteristic fully developed profile of rectangular duct flow: the velocity peaks near the channel center and decreases smoothly toward the walls, forming a curved core region with strong gradients near the boundaries. The symmetric pattern in

the z -direction and the gradual decay toward all walls confirm that the solution captures the expected transverse variations of laminar stratified flow.

F. 1-D and 2-D Stratified Flow: Concentration Profiles

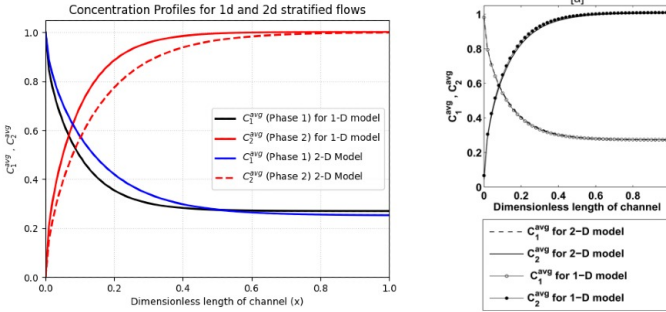


Fig. 7. Average concentration profiles for 1-D and 2-D stratified flow models (parameters corresponding to $\lambda = 0.1$, $k_s = k_{ca} = 0.2703$), compared with the reference plot from Vir *et al.* [1].

Figure 7 shows the cross-sectionally averaged concentrations $C_1^{\text{avg}}(x)$ and $C_2^{\text{avg}}(x)$ for the 1-D and 2-D stratified models. In our results, Phase 1 concentration drops sharply near the inlet, while Phase 2 rises correspondingly—consistent with extraction into the solvent stream.

As expected for $\lambda = 0.1$, the 2-D model exhibits slightly slower equilibration due to additional wall confinement, while the 1-D model converges faster. These trends match the behaviour reported in the reference paper and confirm that, for small aspect ratios, the simpler 1-D formulation provides a good approximation to the full 2-D stratified microchannel.

G. Core–Annular Flow: Concentration Profiles

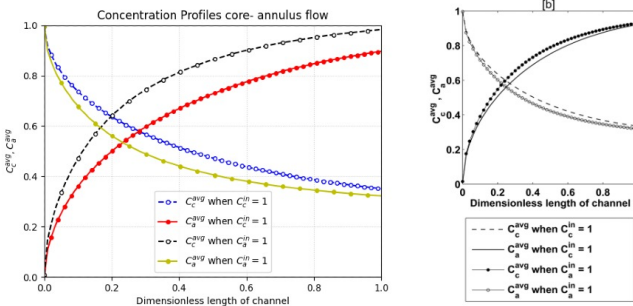


Fig. 8. Average concentration profiles for core–annular flow (parameters corresponding to $\lambda = 0.1$, $k_s = k_{ca} = 0.2703$), compared with the reference plot from Vir *et al.* [1].

Figure 8 shows the evolution of the cross-sectionally averaged concentrations for core–annular flow under the two inlet configurations: carrier entering as the core and as the annulus. Both cases reproduce the characteristic behavior reported in the reference: the phase receiving the carrier shows a monotonic decay of $C_c^{\text{avg}}(x)$, while the solvent-side concentration rises toward equilibrium.

The two configurations also illustrate a key observation: extraction is more effective when the carrier fluid enters as the *annular* phase. This is consistent with the physical interpretation greater wall contact and higher shear in the annulus enhance mass transfer compared to the protected core region.

H. Extraction Performance Metrics

The extraction behaviour of the liquid–liquid systems is quantified using the *extraction ratio* (ER). These metrics are used throughout the validation of the mathematical models and for comparison with the results reported in the literature.

Extraction Ratio: The extraction ratio is defined as the fraction of solute removed from the carrier phase by the solvent phase over the length of the channel. Assuming the inlet concentration in the solvent is zero ($c_{2,\text{in}}^{\text{avg}} = 0$), the extraction ratio is

$$\text{ER} = \frac{c_{2,\text{out}}^{\text{avg}} Q_2}{c_{1,\text{in}}^{\text{avg}} Q_1}. \quad (45)$$

Here, $c_{i,\text{out}}^{\text{avg}}$ denotes the cross-sectional average concentration of solute at the outlet of phase i .

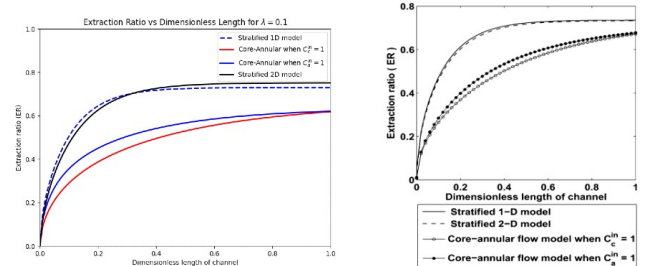


Fig. 9. Extraction ratio (ER) versus dimensionless channel length for $\lambda = 0.1$ ($k_s = k_{ca} = 0.2703$), generated using the same operating conditions as in Vir *et al.*, left

Figure 9 presents the predicted extraction ratio for $\lambda = 0.1$. The ER increases rapidly near the inlet, driven by the large initial concentration difference between the phases, and then gradually approaches a steady value as local equilibrium is attained. The ordering of the curves across the different geometries follows the expected physical trends: the 2-D stratified model gives the highest ER because transverse gradients enhance interfacial transfer, the 1-D model follows closely, and the core–annular configurations show the slowest approach to equilibrium due to their lower effective interfacial area and longer solvent residence times. These behaviours are consistent with the trends reported in the reference study.

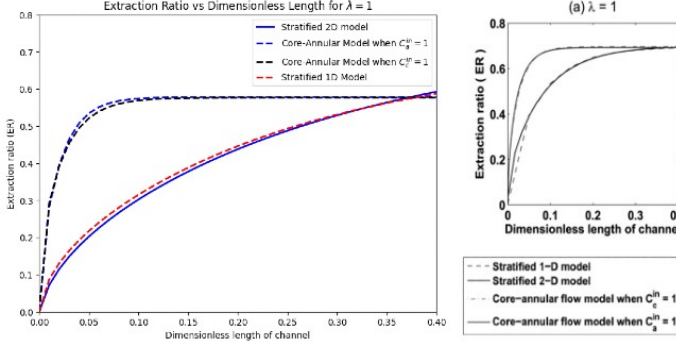


Fig. 10. Comparison of the reconstructed extraction ratio (ER) for $\lambda = 1$ ($k_s = k_{ca} = 0.2703$) with the corresponding reference plot from Vir *et al.* (right).

Figure 10 compares the reconstructed extraction ratio (ER) profiles for $\lambda = 1$ with the reference results reported by Vir *et al.* (2014). All four configurations the stratified 1-D and 2-D models, and the core–annular cases with the carrier occupying either the core or the annulus show the expected rise in ER along the channel, with a rapid increase near the inlet followed by gradual saturation. The reconstructed curves closely follow the trends of the published data, confirming that the velocity fields, species-transport equations, and numerical formulation have been implemented correctly. In agreement with the original study, stratified flow yields the highest extraction performance for $\lambda = 1$, whereas the core–annular configurations show reduced ER due to smaller interfacial area and longer diffusion path lengths.

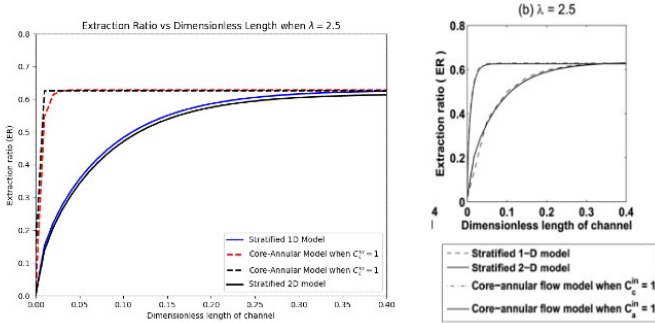


Fig. 11. Comparison of the reconstructed extraction ratio (ER) for $\lambda = 2.5$ ($k_s = k_{ca} = 0.2703$) with the corresponding reference plot from Vir *et al.* (right).

Figure 11 presents the extraction ratio for the case $\lambda = 2.5$. As expected, increasing the aspect ratio enhances transverse mass transfer in the stratified geometries, leading to faster approach toward the equilibrium ER value.

The reconstructed curves closely match the reference trends. For all geometries (1-D, 2-D, and core–annular), the initial rise in ER and the subsequent saturation behaviour follow the same qualitative and quantitative pattern reported in the literature. The separation between the stratified and core–annular curves is also consistent with the original publication.

Slight differences in smoothness originate from discretisation and averaging, but overall the agreement confirms that the implemented models reliably capture the dependence of extraction performance on the channel aspect ratio.

Extraction Ratio for Stratified 2-D Model at Different Aspect Ratios

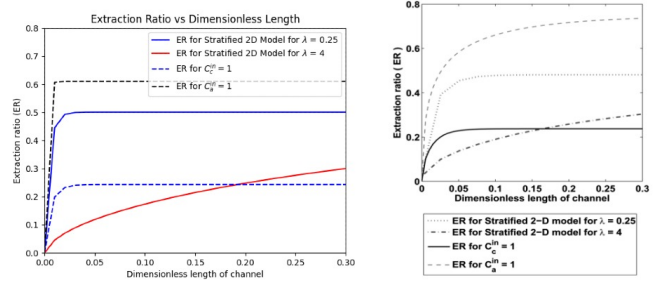


Fig. 12. Comparison of our reproduced extraction–ratio curves (left) with the reference data from Vir *et al.* (right) for two aspect ratios, $\lambda = 0.25$ and $\lambda = 4$.

Figure 12 compares the extraction ratio (ER) for two aspect-ratio cases, $\lambda = 0.25$ and $\lambda = 4$, using the stratified 2-D model. For $\lambda = 0.25$, the ER increases rapidly near the inlet and reaches its equilibrium value early, consistent with the reference result. For $\lambda = 4$, the ER rises more gradually along the channel due to the larger transverse diffusion distance associated with high-aspect-ratio microchannels. The overall ordering of the curves, the growth trends, and the equilibrium limits match the published behaviour in Vir *et al.* (2014), confirming that our reproduced model correctly captures the dependence of extraction performance on channel geometry. Small differences arise from discretization resolution, but they do not alter the physical interpretation.

MASS BALANCE VALIDATION

1D stratified Flows

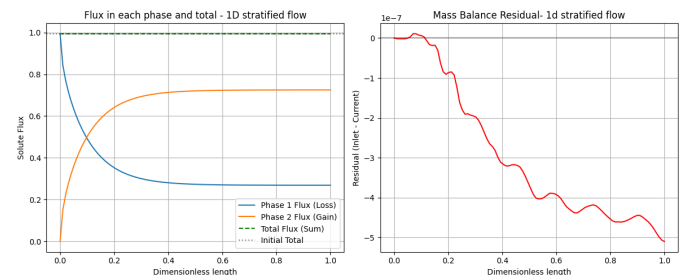


Fig. 13. Mass balance validation of 1D stratified flow

Running Mass Balance Verification for 1-D Stratified Flows(extracted from python)

```

Initial Phase 1 flux: 0.99427506
Initial Phase 2 flux: 0.00000000
    Initial Total flux: 0.99427506
Final Phase 1 flux: 0.26920552
Final Phase 2 flux: 0.72507005
    Final Total flux: 0.99427557
Max Residual Error: 5.10 × 10-7

```

2D stratified Flows

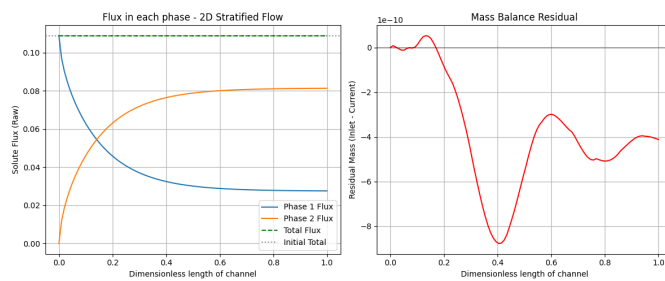


Fig. 14. Mass balance validation for 2D stratified flow

Normalization and Mass Balance Verification for 2d stratified (extracted from python)

Mass Balance Verification

```

Initial Phase 1 Flux: 0.10888503
Initial Phase 2 Flux: 0.00000000
    Initial Total Flux: 0.10888503
Final Phase 1 Flux: 0.02755734
Final Phase 2 Flux: 0.08132769
    Final Total Flux: 0.10888503
Max Residual Error: 8.78 × 10-10

```

Core Annular Flow when $C_c^{in} = 1$

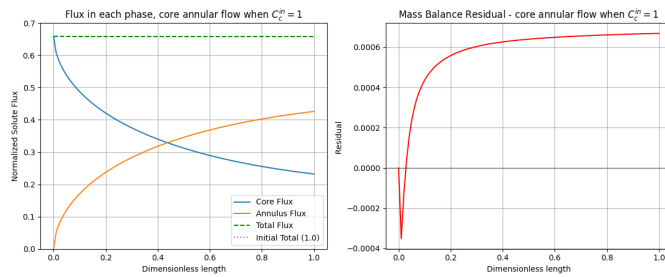


Fig. 15. Core annular flow when $C_c^{in} = 1$

Normalization and Mass Balance Verification for Core annular flow when $C_c^{in} = 1$

```

Initial Core Flux: 0.65814537
Initial Annulus Flux: 0.00074294
    Initial Total Flux: 0.65888831
Final Core Flux: 0.23217268
Final Annulus Flux: 0.42604692
    Final Total Flux: 0.65821960
Max Residual Error: 6.69 × 10-4

```

Core Annular Flow when $C_a^{in} = 1$

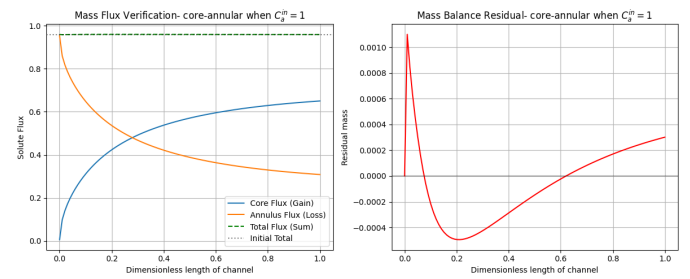


Fig. 16. Core annular when $C_a^{in} = 1$

Mass Balance Verification Results for Core annular flow when $C_a^{in} = 1$

```

Initial Core Flux: 0.00624843
Initial Annulus Flux: 0.95279967
    Initial Total Flux: 0.95904810
Final Core Flux: 0.65025552
Final Annulus Flux: 0.30849150
    Final Total Flux: 0.95874701
Max Residual Error: 1.10 × 10-3

```

Formula used to calculate the Mass Balance Verification:

At each axial location x , the solute flows in the two phases and the cumulative interfacial transfer are used to compute the mass-balance residual (from the project brief):

$$R(x) = \dot{M}_{in} - [Q_1 \bar{c}_1(x) + Q_2 \bar{c}_2(x)] - \int_0^x J(s) ds, \quad (46)$$

where $\dot{M}_{in} = Q_{1,in}$ is the inlet solute flow, $\bar{c}_i(x)$ is the cross-sectional average concentration of phase i , and $J(x)$ is the interfacial flux,

$$J(x) = -D_1 \frac{\partial c_1}{\partial n} \Big|_\Gamma = -D_2 \frac{\partial c_2}{\partial n} \Big|_\Gamma. \quad (47)$$

A consistent numerical solution yields $R(x) \approx 0$ along the channel. The cumulative solute-flow plots show phase 1 losing solute and phase 2 gaining solute, while the total remains nearly constant to a sum of 1. The residual plot confirms conservation, with absolute errors on the order of 10^{-8} – 10^{-7} , well within the acceptable tolerance.

LEARNINGS AND CHALLENGES

Learnings

Some key learnings from the regeneration of graphs were:

- How velocity profile shape extraction performance in stratified and core-annular flows, and the roles of viscosity ratio, holdup, and pressure gradient.
- The usefulness of non-dimensionalisation (Péclet number, viscosity and flow-rate ratios, holdup) in generalizing models across different geometries.
- The role of aspect ratio in selecting which type of flow is best for the highest Liquid-Liquid extraction.
- 1-D approximation of 2-D model is an accurate approximation and can be used interchangeably

Challenges Faced

The project also required addressing several modelling and numerical difficulties:

- The reference paper omits many intermediate derivation steps, so full reductions of Navier-Stokes, non-dimensionalisation, and eigenfunction expansions had to be derived using knowledge from lectures, referenced research papers.
- Reconstructing the published plots required careful numerical implementation, enforcing the boundary/interface conditions.
- Modeling of concentration profiles using the Method of lines method
- Application of method of lines from scratch in python, taking in consideration, the stiff boundary conditions.

These challenges strengthened our theoretical understanding and improved our ability to implement and validate computational models for liquid-liquid extraction in microchannels.

CONCLUSION

In this work, we reconstructed the liquid-liquid extraction behaviour in three microchannel flow configurations—core-annular flow in a circular channel, two-dimensional stratified flow in a rectangular microchannel, and the simplified one-dimensional stratified model. Analytical velocity fields were derived, non-dimensionalized, and implemented together with numerical solutions of the advection-diffusion equations using the Method of Lines.

The reconstructed results showed strong agreement with the reference study by Vir *et al.* [1], validating both the modelling framework and the numerical implementation. Velocity contours, concentration profiles, and extraction ratio metrics reproduced the trends reported in the literature.

We also compared extraction performance across geometries and operating conditions. Stratified flow exhibited higher extraction when the core holdup was below the critical value, primarily due to larger interfacial area and shorter diffusion paths. Conversely, core-annular flow outperformed stratified flow when the core holdup was high or when the carrier flowed in the slower annular region. The 1-D model was consistent even at moderate aspect ratios.

Overall, this project deepened our understanding of microchannel hydrodynamics, interfacial mass transfer, and the interplay of diffusion, convection, and holdup.

ACKNOWLEDGMENTS

We, the members of Group 14 thank Prof. Karthik Subramanian Pushpavanam for his guidance and insightful discussions throughout the project.

We also express our gratitude to Prof. S. Pushpavanam (IIT Madras) for his lecture series “*Multiphase Flows: Analytical Solutions and Stability Analysis*”, which provided essential theoretical foundations for understanding stratified and core-annular flows.

REFERENCES

- [1] A. B. Vir, A. S. Fabiyan, J. R. Picardo, and S. Pushpavanam, “Performance Comparison of Liquid-Liquid Extraction in Parallel Microflows,” *Industrial & Engineering Chemistry Research*, vol. 53, no. 21, pp. 8171–8181, 2014.
- [2] B. Malengier, S. Pushpavanam, and S. D’haeyer, “Optimizing performance of liquid-liquid extraction in stratified flow in micro-channels,” *Journal of Micromechanics and Microengineering*, vol. 21, no. 11, pp. 115030–115030, Oct. 2011, doi: 10.1088/0960-1317/21/11/115030.
- [3] J. R. Picardo and S. Pushpavanam, “On the Conditional Superiority of Counter-Current over Co-Current Extraction in Microchannels,” *Microfluidics and Nanofluidics*, vol. 15, pp. 701–713, 2013.
- [4] S. Pushpavanam and B. Malengier, “Comparison of Co-Current and Counter-Current Flow Fields on Extraction Performance in Micro-Channels,” *Advances in Chemical Engineering and Science*, vol. 2, no. 2, pp. 309–320, 2012, doi: 10.4236/aces.2012.22036.
- [5] S. Pushpavanam, “Introduction and overview” YouTube, 2016. [Online]. Available: <https://youtu.be/dYvgdN3YRAM>
- [6] S. Pushpavanam, “Two-Phase Flow: Pressure Drop and Holdup Analysis,” YouTube, 2016. [Online]. Available: <https://shorturl.at/frW0t>

PYTHON FILE (DRIVE LINK)

Attached python code (.py format)

Attached python code (.ipynb format)